Directly synthesized nitrogen-doped microporous carbons from polybenzoxazine resins for carbon dioxide capture†

Jia-Yu Wu, Mohamed Gamal Mohamed and Shiao-Wei Kuo [ID] *

In this study, nitrogen-doped microporous carbons, with potential use as capturers for CO_2, were synthesized directly from two new benzoxazines (BZCN and BZPh)—prepared from two phenols (phenol and 4-cyanophenol, respectively), CH_2O, and 1,3,5-tris(4-aminophenoxy)benzene (TPhA)—through thermal curing, carbonization, and KOH activation. FTIR and NMR spectroscopy confirmed the corresponding chemical structures; temperature-dependent FTIR spectroscopic and DSC analyses revealed the thermal curing behavior of the ring opening polymerizations of these two new benzoxazine monomers. Of the two benzoxazines, the nitrile-functionalized benzoxazine BZCN, derived from 4-cyanophenol, exhibited —after thermal curing, carbonization, and KOH activation—enhanced thermal properties, cross-linking density, and CO_2 capture, based on thermogravimetric analysis, dynamic mechanical analysis, and Brunauer–Emmett–Teller (BET) analysis. Analyses using Raman spectroscopy, wide-angle X-ray diffraction, transmission electron microscopy, the BET method, and X-ray photoelectron spectroscopy provided information about the microporous structures and surface areas of these two highly ordered microporous N-doped carbon materials.

Introduction

Porous carbon materials with large surface areas and pore volumes are environmentally friendly materials having great potential in electrochemical energy storage (*e.g.*, lithium-ion batteries), supercapacitors, and gas storage (*e.g.*, SO_2 adsorption and CO_2 capture) applications.[1–8] In addition, nitrogen (N)-containing porous carbon materials have been the subject of considerable research efforts for the past three decades ever since it was discovered that the introduction of N heteroatoms can enhance the polarity and improve the chemical properties favorable for CO_2 capture;[9–11] that is, N-containing porous carbon materials are stronger Lewis bases that interact more strongly with acidic CO_2 gas and, thereby, enhance the adsorption capacity.[12,13]

Several approaches have been reported for the preparation of N-containing porous carbon materials, including (i) reactions of porous carbons with N-containing materials (*e.g.*, melamine), (ii) co-carbonizations of N-containing materials with N-free precursors, and (3) direct carbonizations of

raw materials containing N atoms.[14–18] Several reported N-containing porous carbons have displayed enhanced CO_2 capture ability, with the most approaches for their preparation involving the use of N-containing polymers (*e.g.*, polyacrylonitrile, polyaniline, polypyrrole, polyindole) as carbon precursors.[19–23] In addition to those N-containing organic polymers, a new class of thermosetting polymers, polybenzoxazines, have N atoms and display high char yields and high thermal stability, with the attraction of flexible molecular design.[24–31] Many reports describe the improved performance of polybenzoxazines after incorporating reactive functional groups that increase their crosslinking densities.[32–37] Nevertheless, only a few reports describe the preparation of polybenzoxazines as carbon precursors. For example, Hao and co-workers used poly(benzoxazine-*co*-resol) polymers to prepare N-containing porous carbons displaying excellent CO_2 capture ability,[38] while Li *et al.* developed a polybenzoxazine from a nitrile-functionalized benzoxazine monomer (prepared from melamine, –CH_2O, and 4-cyanophenol) which also exhibited outstanding CO_2 capture ability.[39–41]

In this study, we replaced the melamine used by Li *et al.* with 1,3,5-tris(4-aminophenoxy)benzene (TPhA) as the amine derivative for the synthesis of the benzoxazine monomer, expecting that the larger molecular size of TPhA would result in larger pores in the final N-containing porous carbons. We investigated the effect of the nitrile-functionalized benzoxazine

Department of Materials and Optoelectronic Science, Center for Functional Polymers and Supramolecular Materials, National Sun Yat-Sen University, Kaohsiung, 804, Taiwan. E-mail: kuosw@faculty.nsysu.edu.tw
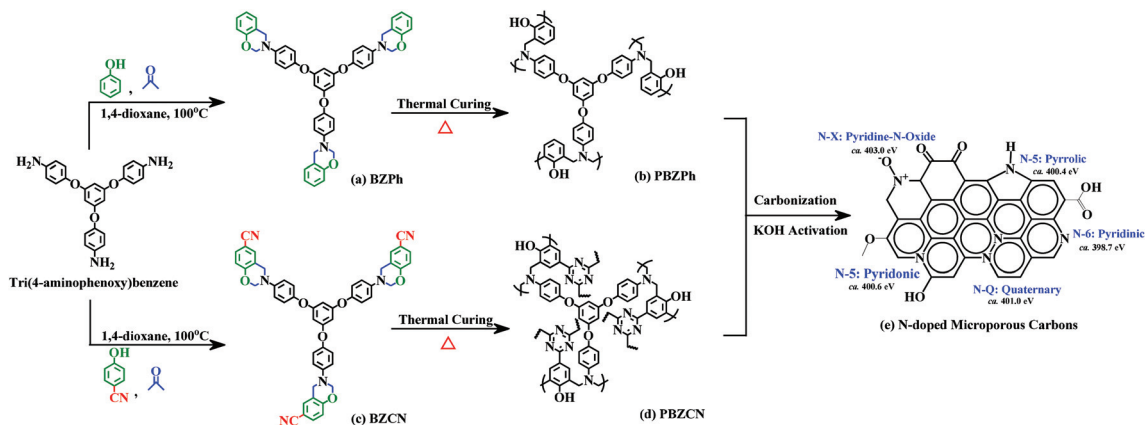
Scheme 1 Synthesis of benzoxazine monomers (a) BZPh and (c) BZCN; thermally activated ring-opening polymerization giving the polybenzoxazines (b) PBZPh and (d) PBZCN; and (e) carbonization and KOH activation of the N-doped microporous carbons.

monomer on the resulting N-containing microporous carbons by using 1,3,5-tris[4-(2H-benzoxazinyl)phenoxy]benzene (BZPh, no nitrile group) and 3,3′,3″-[(benzene-1,3,5-triyltris(oxy))tris(benzene-4,1-diyl)]tris(3,4-dihydrobenzoxazine-6-carbonitrile) (BZCN, with nitrile group) as monomers (Scheme 1). To the best of our knowledge, we are the first to investigate the nitrile group effect on the benzoxazine matrix leading to N-doped microporous carbons. Fourier transform infrared (FTIR) and nuclear magnetic resonance (NMR) spectroscopy confirmed the chemical structures of these two new benzoxazine monomers. We used differential scanning calorimetry (DSC), FTIR spectroscopy, thermogravimetric analysis (TGA), and dynamic mechanical analysis (DMA) to investigate the thermal curing behavior of these benzoxazine monomers. The microporous structures, surface areas, and CO_2 adsorption behaviors of these highly ordered microporous N-doped carbons were investigated using wide-angle X-ray diffraction (WAXD), transmission electron microscopy (TEM), the Brunauer–Emmett–Teller (BET) method, Raman spectroscopy, and X-ray photoelectron spectroscopy (XPS).

Experimental section

Materials

Phloroglucinol, 4-chloro-4-nitrobenzene, potassium carbonate (K_2CO_3), potassium hydroxide (KOH), phenol, 4-cyanophenol, paraformaldehyde, and ethyl acetate were purchased from Acros. Palladium on activated carbon (Pd/C), 1,4-dioxane, N,N-dimethylformamide (DMF), dichloromethane (CH_2Cl_2), tetrahydrofuran (THF), chloroform ($CHCl_3$), ethanol (EtOH), and hydrazine monohydrate (N_2H_4) were purchased from Alfa Aesar. 1,3,5-Tris(4-aminophenoxy)benzene was synthesized using a previously reported procedure (Fig. S1 and S2†).[29]

1,3,5-Tris[4-(2H-benzoxazinyl)phenoxy]benzene (BZPh)

A solution of TPhA (2.00 g, 5.01 mmol), phenol (1.41 g, 15.0 mmol), and paraformaldehyde (0.920 g, 30.0 mmol) in

1,4-dioxane (80 mL) was heated at 100 °C under N_2 for 5 h. The rotary evaporation of the solvent and precipitation in MeOH provided a powder. After few steps of purification, the product was dried at 45 °C under vacuum to afford a yellow powder.

3,3′,3″-[(Benzene-1,3,5-triyltris(oxy))tris(benzene-4,1-diyl)] tris (3,4-dihydrobenzoxazine-6-carbonitrile) (BZCN)

A solution of 4-cyanophenol (1.79 g, 15.0 mmol), CH_2O (0.920 g, 30.0 mmol), and TPhA (2.00 g, 5.01 mmol) in 1,4-dioxane (80 mL) was heated at 100 °C under N_2 for 5 h. The solvent was remove by rotary evaporation and then MeOH precipitation was used to obtain the powder. After several purification steps, the final product was dried under vacuum at 45 °C to obtain the yellow powder.

Thermal curing, carbonization, and activation of BZPh and BZCN monomers

An aluminum pan was charged with a desired amount of a benzoxazine monomer and heated stepwise in an oven at 100, 150, 180, 200, and 250 °C for 2 h. After thermal curing, the sample was calcined in a tubular furnace at a heating rate of 5 °C min^{-1} up to a temperature of 600 °C for 6 h, mixed in aqueous KOH solution [KOH/powder, 2 : 1 (w/w)] at room temperature for 24 h and then, after removing the water, activated at 600 °C for 2 h in a tubular furnace under a flow of N_2. The products were repeatedly washed with deionized H_2O until the pH of the filtrate reached ca. 7, then dried at 120 °C.

Characterization

^{1}H and ^{13}C NMR spectra were recorded using an INOVA 500 instrument with DMSO-d_6 as the solvent, operated at 500 and 125 MHz, respectively. FTIR spectra of all benzoxazine samples were recorded using a Bruker Tensor 27 FTIR spectrophotometer and the typical KBr disk method with 32 scans at a spectral resolution of 4 cm^{-1}; all prepared samples were sufficiently thin to obey the Beer–Lambert law. The dynamic thermal curing of the samples was monitored at elevated temperatures

using a cell mounted in the temperature-controlled compartment of the FTIR spectrophotometer. Because of the presence of hydroxyl groups for all samples, a N_2 flow was used to keep the sample films dry during the measurement. The thermal properties and dynamic curing behavior of all benzoxazine samples with a 5–7 mg sample in the DSC sample cell were determined using a TA Q-20 DSC apparatus, with a heating scan from 30 to 350 °C at 20 °C min^{-1} under a N_2 atmosphere (100 mL min^{-1}). The thermal stabilities of all the benzoxazine samples with a 5–7 mg sample were measured using a TA Q-50 TGA apparatus, with heating from 30 to 800 °C at 20 °C min^{-1} under a N_2 atmosphere (100 mL min^{-1}). The glass transition temperatures of the thermally cured benzoxazine samples were determined using a PerkinElmer Instruments DMA 8000 apparatus operated in the tension mode from 30 to 400 °C (heating rate: 2 °C min^{-1}; frequency: 1 Hz). The loss tangent (tan δ) was recorded to determine the glass transition temperature automatically. Raman spectra were recorded at room temperature using a Jobin–Yvon T6400 micro-Raman apparatus with a He–Cd laser as the excitation source (325 nm). High-resolution solid state ^{13}C NMR spectra were recorded at room temperature using a Bruker DSX-400 spectrometer, operated at a resonance frequency for ^{1}H (399.53 MHz) and ^{13}C (100.47 MHz). All NMR spectra were measured using broad band proton decoupling and a normal cross-polarization pulse sequence. In addition, a magic-angle spinning (MAS) rate of 5.4 kHz was used to eliminate resonance broadening because of the anisotropy of the chemical shift tensors. XPS was performed using the Mg Kα radiation from the double anode at 50 W. The related binding energies of all benzoxazine samples in the high-resolution spectra were calibrated by using C 1s at 284.6 eV. WAXD data of all benzoxazine samples were measured using the BL17A1 wiggler beamline of the National Synchrotron Radiation Research Center (NSRRC), Taiwan, with a wavelength (λ) of 1.33001 Å used from the monochromated beam based on a triangular bent Si (111) single crystal. The TEM images of N-doped microporous carbons were recorded using a JEOL-2100 transmission electron microscope operated at an accelerating voltage of 200 kV. The ultrathin sections of all samples were placed on Cu grids coated with carbon-supporting films. The CO_2 adsorption isotherms were determined using an ASAP 2020 analyzer at 25 °C. The samples of N-doped microporous carbons were degassed at 150 °C for 2 h prior to the measurement. The BET method was used to measure the specific surface areas, pore size distributions, and pore volumes from the adsorption branches of the isotherms.

Results and discussion

Synthesis of BZPh and BZCN monomers

In this study, we synthesized the benzoxazine monomers BZPh and BZCN to vary the N atom contents in the final N-containing microporous carbons; their structures were confirmed using NMR and FTIR spectroscopy. Fig. 1 presents the
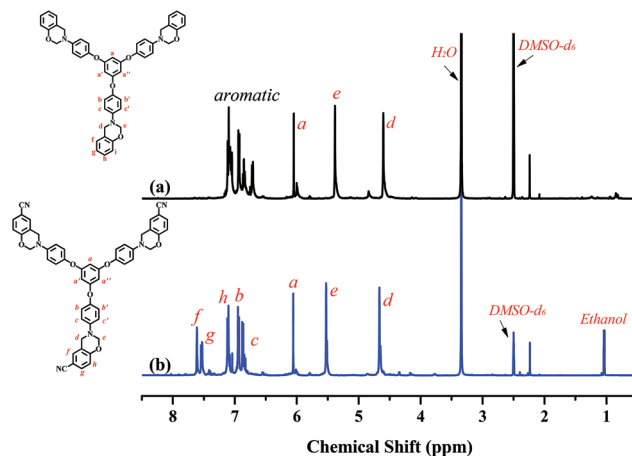

Fig. 1 ^{1}H NMR spectra of the benzoxazine monomers (a) BZPh and (b) BZCN.

^{1}H NMR spectra of BZPh and BZCN. Two clear sharp peaks appear at 4.60 and 5.38 ppm with an integrated ratio of 1 : 1 in Fig. 1(a), corresponding to the CC**H**$_2$N and OC**H**$_2$N units of BZPh. Similarly, the spectrum of BZCN also features two sharp peaks at 4.66 and 5.52 ppm with an integrated ratio of 1 : 1 [Fig. 1(b)] for the corresponding CC**H**$_2$N and OC**H**$_2$N units. Furthermore, the spectrum of BZCN also features signals for aromatic protons (peaks **f** and **g**) arising from the influence of the 4-cyanophenol group. All other peaks are assigned in Fig. 1. Fig. 2 displays the ^{13}C NMR spectra of BZPh and BZCN. Two characteristic peaks at 49.57 and 79.63 ppm represent the CC**H**$_2$N and OC**H**$_2$N nuclei of BZPh with the other aromatic signals appearing from 100.99 to 160.79 ppm [Fig. 2(a)]. Similarly, the spectrum of BZCN displays two characteristic peaks at 48.84 and 80.88 ppm [Fig. 2(b)] representing its corresponding CC**H**$_2$N and OC**H**$_2$N nuclei. In addition, the spectrum of BZCN displays additional signals (peak **l** at 103.28 ppm; peak **o** at 117.82 ppm) arising from the 4-cyano-
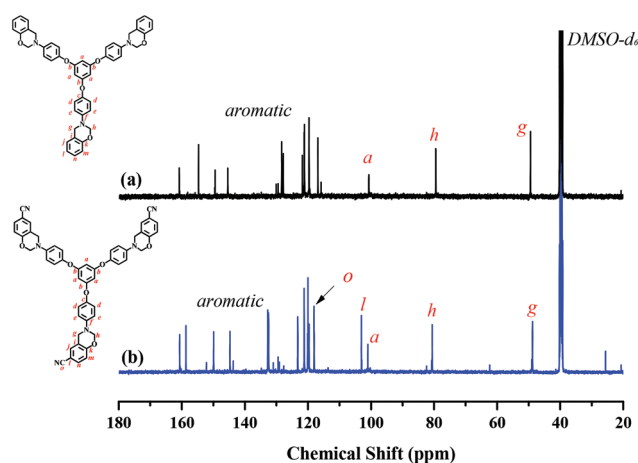

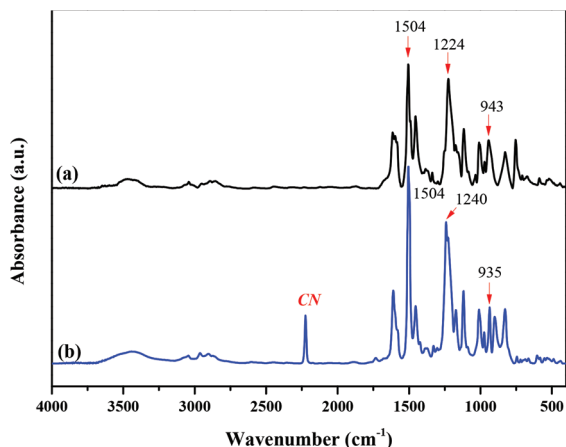**Fig. 2** ^{13}C NMR spectra of the benzoxazine monomers (a) BZPh and (b) BZCN.

Fig. 3 FTIR spectra of the benzoxazine monomers (a) BZPh and (b) BZCN.

Fig. 4 (A) DSC thermograms and (B) FTIR spectra of the BZPh monomer after curing at various temperatures.

Fig. 5 (A) DSC thermograms and (B) FTIR spectra of the BZCN monomer after curing at various temperatures.

phenol group. Fig. 3 displays the FTIR spectra of BZPh and BZCN recorded at room temperature. The characteristic adsorption peaks of the benzoxazine moieties of BZPh are located at 1224 cm^{-1} (asymmetric COC stretching) and 943 and 1504 cm^{-1} (vibrations of the trisubstituted benzene ring) in Fig. 3(a), consistent with the successful benzoxazine ring formation. Similarly, the spectrum of BZCN also displays [Fig. 3(b)] signals for the benzoxazine moieties at 1240 cm^{-1} (asymmetric COC stretching) and 935 and 1504 cm^{-1} (vibrations of the trisubstituted benzene ring), consistent with successful benzoxazine ring formation. More importantly, a signal for a cyano (CN) group was present at 2224 cm^{-1} in the spectrum of BZCN, but it was absent in the spectrum of BZPh. Based on these NMR and FTIR spectroscopic analyses, we conclude that the benzoxazine monomers BZPh and BZCN were synthesized successfully with high purity.

Thermal behavior of BZPh and BZCN monomers and the activation process

We combined DSC and FTIR spectroscopic analyses to investigate the thermal curing behavior of the BZPh and BZCN monomers. Fig. 4(A) presents the DSC thermograms of the uncured BZPh monomer; the sharp exothermic peak was observed at 257 °C and the enthalpy of the thermal curing reaction was 247.2 J g^{-1}. Both these values decreased gradually upon increasing the thermal curing temperature, with the exothermic peak disappearing completely after thermal curing at 250 °C, suggesting a fully thermally cured state for the BZPh-type polybenzoxazine. We also recorded FTIR spectra to monitor the thermal ring-opening polymerization of the BZPh monomer at various temperatures. The characteristic adsorption peak of the benzoxazine group of the BZPh monomer, located at 943 cm^{-1}, almost disappeared completely after thermal curing at 250 °C, as revealed in Fig. 4(B), consistent with the DSC analyses in Fig. 4(A).

Fig. 5(A) displays the DSC thermograms of the uncured BZCN monomer; the sharp exothermic peak was observed at
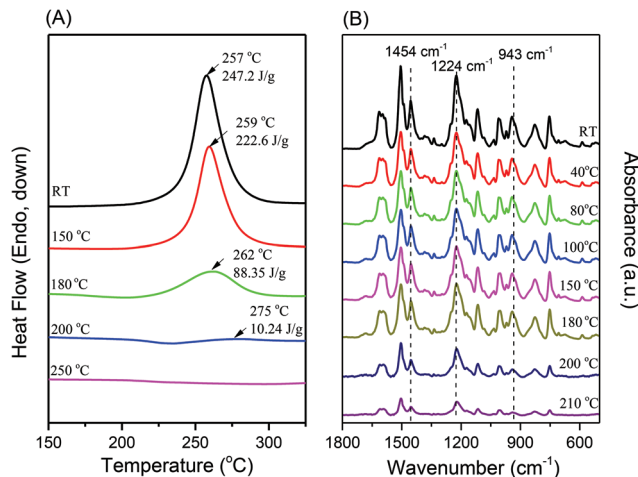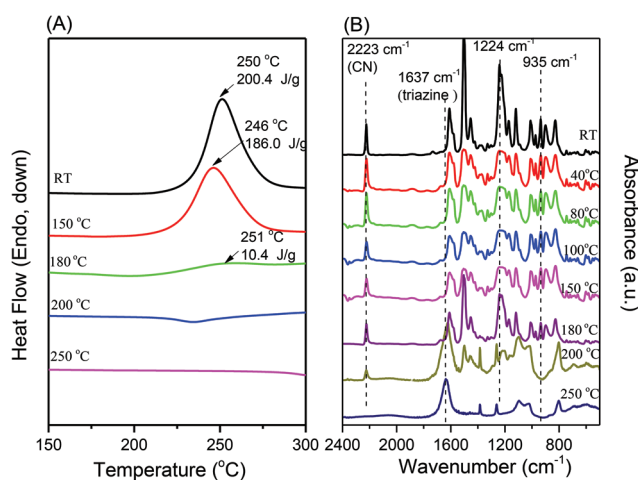
250 °C and the enthalpy of the thermal curing reaction was 200.4 J g^{-1}. Again, both these values decreased gradually upon increasing the thermal curing temperature, with the exothermic peak disappearing completely after thermal curing at only 200 °C, suggesting the fully thermal curing state of the BZCN-type polybenzoxazine. Thus, the curing temperature for the BZCN monomer (250 °C) was lower than that for the BZPh monomer (257 °C), presumably due to the basicity of the CN group; that is, the CN moiety might act as a basic catalyst to lower the thermal curing temperature. Most importantly, the CN group could further transform into a triazine ring through thermal polymerization at a higher temperature, thereby forming an additional extended two-dimensional (2D) framework to further increase the crosslinking density of the BZCN-type polybenzoxazine, as displayed in Fig. 5(B). The characteristic benzoxazine peak of BZCN, located at 935 cm^{-1}, disappeared completely from the FTIR spectrum after thermal
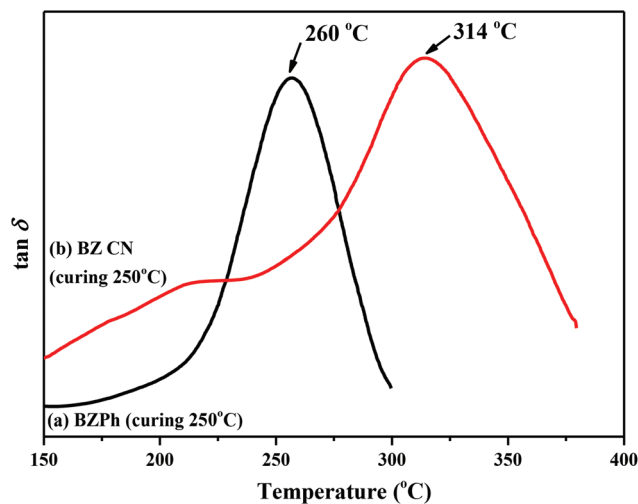
Fig. 6 DMA thermograms of the polybenzoxazines (a) BZPh and (b) BZCN after thermal curing at 250 °C.

Fig. 7 TGA thermograms of the monomers (a) BZPh and (b) BZCN; after thermal curing (at 250 °C) of the polybenzoxazines (c) PBZPh and (d) PBZCN; after carbonization (e) BZPh-C, and (f) BZPh-C; and KOH activation of (g) BZPh-A and (h) BZCN-A under a N_2 atmosphere.

curing at only 200 °C, consistent with the DSC analysis [Fig. 5 (A)]. In addition, the characteristic peak at 2224 cm^{-1}, corresponding to the CN group, disappeared completely after thermal curing at 250 °C, with two new characteristic peaks appearing at 1637 and 1385 cm^{-1}, consistent with successful trimerizations forming triazine rings.[39–42] We used DMA to investigate the glass transition temperature behavior of the BZPh- and BZCN-type polybenzoxazines after thermal curing at 250 °C (Fig. 6). The value of T_g from the loss tan δ peak of the BZCN-type polybenzoxazine (T_g = 314 °C) was higher than that for the BZPh-type polybenzoxazine (T_g = 260 °C), indicating that the additional extended 2D framework arising from the triazine rings of the BZCN-type polybenzoxazine increased the crosslinking density when compared with that of the BZPh-type polybenzoxazine and, thereby, increased the value of T_g.

We used TGA analyses to investigate the thermal curing, carbonization, and activation processes of the BZPh- and BZCN-type polybenzoxazines under a N_2 atmosphere, as displayed in Fig. 7. Both the thermal decomposition temperature (T_{d5}) and char yield increased after thermal curing for both types of polybenzoxazines, the result of an increasing crosslinking density. Furthermore, the BZCN-type polybenzoxazine had higher values of T_d (393 °C) and char yield (70 wt%) after thermal curing, due to the additional extended 2D framework of triazine rings [Fig. 7(d)], than those of the BZPh-type polybenzoxazine [T_d = 380 °C; char yield = 65 wt%; Fig. 7(c)] lacking triazine rings. After the carbonization and activation process, the values of T_d and char yields increased further for BZPh-C and BZCN-C, even BZPh-A and BZCN-A because of framework carbonization and activation. Nevertheless, the BZCN-type polybenzoxazine [Fig. 7(h)] had a lower value of T_d (681 °C) and a lower char yield (90 wt%) than did the BZPh-type polybenzoxazine [T_d = 726 °C; char yield = 92 wt%; Fig. 7(g)], presumably due to the decomposition of more N species in the former system. Overall, the BZPh- and BZCN-
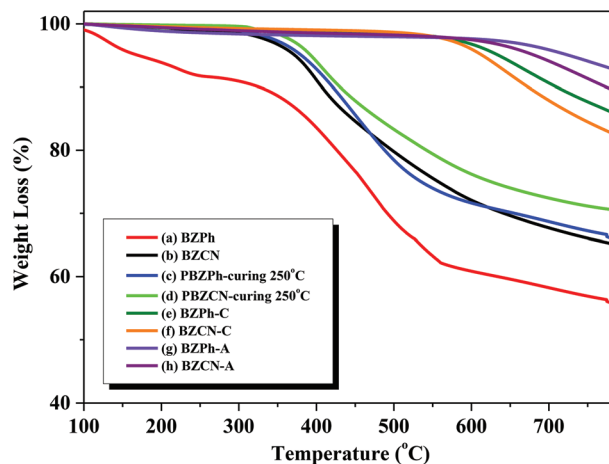
type polybenzoxazines exhibited outstanding thermal stability after the carbonization and activation processes.

Fig. 8(a)–(d) present characterization data of both the BZPh and BZCN monomers before and after performing the thermal curing, carbonization, and activation processes. The characteristic adsorption peaks of the benzoxazine groups at 943 [Fig. 8(a)] and 935 [Fig. 8(c)] cm^{-1} disappeared after the thermal curing, carbonization, and activation processes. The spectra of the activated samples BZPh-A and BZCN-A feature broad bands because of the strong absorption of carbon, with a broad band near 3445 cm^{-1} representing OH stretching. The signals for the aromatic rings appeared in the range 1500–1620 cm^{-1} for the BZPh-A sample [Fig. 8(b)]; for the BZCN-A sample [Fig. 8(d)], the signal for the CN group at
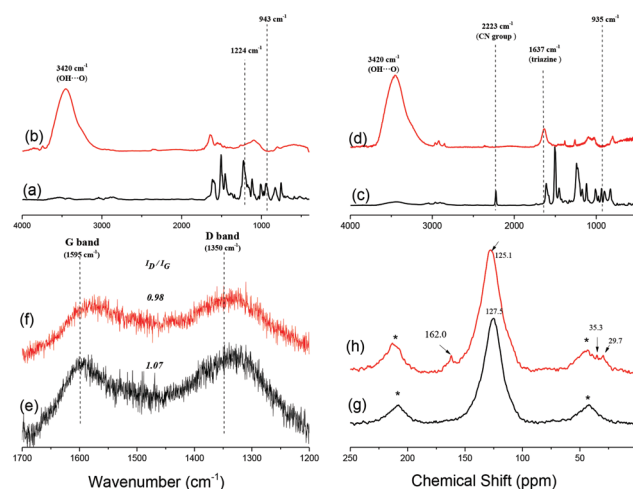

Fig. 8 FTIR spectra of the monomers (a) BZPh and (c) BZCN and after carbonization and KOH activation of (b) BZPh-A and (d) BZCN-A; Raman spectra of (e) BZPh-A and (f) BZCN-A; solid state NMR spectra of (g) BZPh-A and (h) BZCN-A.

2223 cm^{-1} disappeared and while peaks appeared at 1637 cm^{-1} representing the NH absorption and aromatic ring stretching, at 1385 cm^{-1} for the C–N stretching vibration, at 1100 cm^{-1} for the C–O stretching vibration, and weakly near 800 cm^{-1} for the C–H or N–H out-of-plane vibration. All of the FTIR spectra indicate the existence of N–H, C–N, and C–O species in the activated samples. Fig. 8(e) and (f) present the Raman spectra of BZPh-A and BZCN-A samples over the range of 1200 to 1700 cm^{-1}. Two strong peaks appeared for these two carbon materials: a D-band (ca. 1350 cm^{-1}) and a G-band (ca. 1595 cm^{-1}). D-bands typically correspond to disorder and imperfect structures arising from turbostratic carbon layers, while G-bands are usually due to the vibrations of in-plane displaced carbon atoms in the graphite crystallites.[42–45] Therefore, the ratio of I_D to I_G can be a reference for understanding the degree of graphitization of carbon materials. The value of the I_D/I_G ratio for the BZPh-A carbon material was 1.07; it was 0.98 for the BZCN-A carbon material. Thus, the degree of graphitization of the BZCN-A carbon material was higher than that of the BZPh-A carbon materials, presumably because the CN units enhanced the fraction of graphite ferrous carbon atoms. Fig. 8(g) and (h) display the solid state NMR spectra of the BZPh-A and BZCN-A carbon materials. The spectra of both samples feature broad peaks arising from the aromatic carbon nuclei in the range 100–150 ppm; in addition, the spectrum of the BZCN-A carbon material displays extra peaks at 162.0, 35.3, and 29.7 ppm, presumably corresponding to C=O (or C=N), C–N (or C–O), and C–H units.

Table 1 summarizes the chemical compositions, determined through XPS analyses, of the BZPh- and BZCN-type polybenzoxazines (PBZPh and PBZCN); the BZPh-C and BZCN-C carbon materials obtained after the carbonization of PBZPh and PBZCN and the BZPh-A and BZCN-A carbon materials. The N content for PBZCN was higher than that for the PBZPh polybenzoxazine, due to the extra CN units in the BZCN-type polybenzoxazine. Although carbonization would decrease the N contents in these types of polybenzoxazines, further activation enhanced the N contents in both the BZPh-A and BZCN-A carbon materials. We observed high N (5.0 and 5.6 wt%) and O (17.6 and 18.0 wt%) concentrations for the BZPh-A and BZCN-A carbon materials, respectively. Those heteroatoms could arise directly from the intrinsic N and O atom components in the BZPh and BZCN monomers (Scheme 1). More importantly, we had increased the N atom
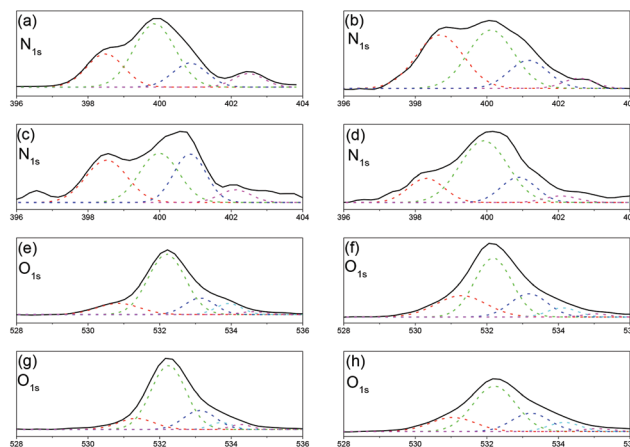

Fig. 9 XPS spectra (N 1s and O 1s orbitals) of (a and e) BZPh-C, (b and f) BZPh-A, (c and g) BZCN-C, and (d and h) BZCN-A samples.

content through the molecular design of the BZCN monomer. We suspected that the N and O heteroatoms in the carbon materials would improve the CO$_2$ adsorption capacity. Fig. 9 presents XPS analyses which we used to realize the types of N and O species. Four major types of N species were distinguishable on the surface of the N-containing carbon material [Scheme 1(e)]: oxidized N (N–X at 403.0 eV), quaternary-N (N–Q at 401.0 eV), pyrrolic-N (N-5 at 400.4 eV), and pyridinic-N (N-6 at 398.7 eV),[39–41] as determined from the curve fitting results in Fig. 9(a)–(d) and Table 2. The total fractions of N-5 and N-6 species increased after performing the activation process for the BZPh-A and BZCN-A carbon materials. For both the BZPh-A (78.77%) and BZCN-A (77.56%) carbon materials, these fractions predominated after the activation process; indeed, the fractions of N-5 and N-6 units in these N-containing microporous carbon materials derived from polybenzoxazines were higher than those of other N-rich carbon materials.[36–38] From the O$_{1s}$ spectra, we could also distinguish the carbon materials present on the surface, including quinone (531.3 eV), C=O (532.3 eV), C–O (533.3 eV), C–OH (534.2 eV),[36–38] and adsorbed H$_2$O (535.9 eV), as determined from the curve fitting results in Fig. 9(e)–(h) and Table 2. Although the fractions of the quinone and C–O units increased after performing the activation process for both the BZPh-A and BZCN-A carbon materials, the fractions of C=O and C–OH units remained

Table 1 Thermal stability, XPS analysis, surface area, and CO$_2$ uptake for all samples used in this study

| Samples | T_g (°C) | T_d (°C) | Char yield (wt%) | XPS analysis (%) | | | S_{micro} (m^2 g^{-1}) | CO$_2$ uptake (mmol g^{-1}) |
				C	O	N		
PBZPh	260	380	65.0	73.7	25.4	0.9	—	—
PBZCN	314	393	70.0	74.6	22.0	3.4	—	—
BZPh-C	—	635	85.7	77.9	20.3	1.8	434	—
BZCN-C	—	614	82.5	76.1	21.8	2.2	541	—
BZPh-A	—	726	92.0	77.4	17.6	5.0	1667	1.44
BZCN-A	—	681	90.0	76.4	18.0	5.6	1866	2.82

Table 2 Area fractions of N_{1s} and O_{1s} spectra, based on the curve fitting data in Fig. 9

| Sample	N species				O species				
	N-6	N-5	N–Q	N–X	Quinone	C=O	C–O	C–OH	H_2O
BZPh-C	24.31	51.28	16.25	8.16	13.49	62.39	13.87	8.11	2.14
BZPh-A	38.27	40.50	16.44	4.79	24.05	48.83	19.26	6.12	1.74
BZCN-C	31.13	34.14	27.65	7.08	11.42	63.59	17.52	4.47	3.00
BZCN-A	17.61	59.95	18.04	4.40	17.42	53.06	19.06	8.00	2.46

greater than 54.95 and 61.06% of the total oxygen species, potentially contributing greatly to CO_2 capture or electrode applications.

### WAXD, TEM, and BET analyses of BZPh-A and BZCN-A carbon materials

Fig. 10 presents the WAXD patterns of the BZPh and BZCN monomers, the BZPh- and BZCN-type polybenzoxazines (PBZPh and PBZCN, respectively), and the BZPh-A and BZCN-A carbon materials. The patterns of the BZPh [Fig. 10(a)] and BZCN [Fig. 10(d)] monomers reveal highly ordered hexagonal packing cylindrical structures, identified from the definitive $1 : \sqrt{4} : \sqrt{7} : \sqrt{9}$ ratio of their diffraction peaks. The first diffraction peak was observed at a value of q^* of 0.418 A^{-1}, corresponding to a d-spacing of 1.5 nm [Fig. 10(a) and (d)]. After thermal curing of these two monomers, the patterns of both PBZPh and PBZCN retained the first diffraction peak at a value of q^* of 0.418 A^{-1}, but the content of highly ordered hexagonal packing cylindrical structures decreased, presumably because the electron density difference became smaller after thermal curing [Fig. 10(b) and (e)]. More interestingly, the apparent reflections with $1 : \sqrt{4} : \sqrt{7} : \sqrt{9}$ reflection ratios reappeared after performing the carbonization and activation processes for the BZPh-A and BZCN-A carbon materials, revealing their

highly ordered hexagonal cylindrical structures, with the first diffraction peak maintained at a value of q^* of 0.418 A^{-1}, corresponding to a d-spacing of 1.5 nm [Fig. 10(c) and (f)]. In addition, the patterns of the BZCN-A carbon material featured extra peaks at higher diffraction angles, with the d-spacing of 0.34 nm possibly representing the inter-layer distance of graphite.

Fig. 11(a) and (d) present CO_2 adsorption isotherms, recorded at 25 °C, for the BZPh-A and BZCN-A microporous carbon materials. We observed rapid increases in the isothermal curves at values of P/P_0 of less than 0.05, suggesting representative type-I isotherms, based on IUPAC classification, for both the BZPh-A and BZCN-A microporous carbon materials.[46] The surface areas of the BZPh-A and BZCN-A microporous carbon materials were 1667 and 1866 m^2 g^{-1}, respectively. The pore sizes and porous distributions were determined based on the Dubinin's pore-volume-filling theory [Fig. 11(b) and (e)]; the average pore sizes were 1.64 nm for the BZPh-A microporous carbon material and 1.68 nm for the BZCN-A microporous carbon material, consistent with the TEM images [Fig. 11(c) and (f)]. The short-range order of the porous structures and pore sizes of approximately 1.5–2 nm were determined from the TEM images. Based on the WAXD analyses in Fig. 10, we calculated the cell parameter a from the equation
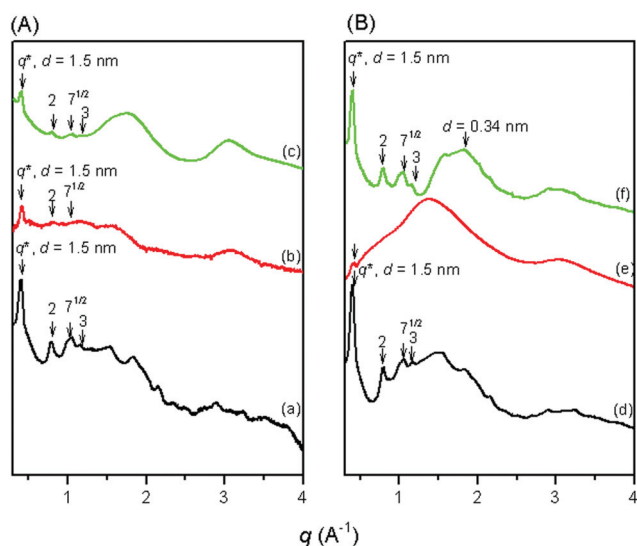
Fig. 10 WAXD patterns of (a) the BZPh monomer, (b) PBZPh, (c) BZPh-A, (d) BZCN monomer, (e) PBZCN, and (f) BZCN-A.
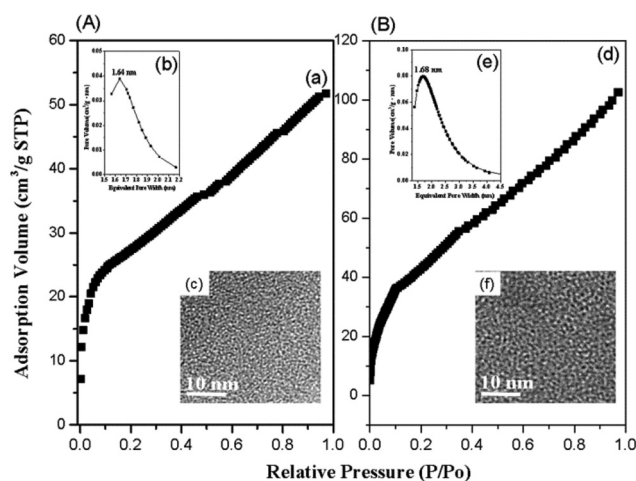
Fig. 11 (A) (a) CO_2 adsorption isotherms recorded at 25 °C, (b) pore size distribution, and (c) TEM image of the BZPh-A sample. (B) (d) CO_2 adsorption isotherms recorded at 25 °C, (e) pore size distribution, and (f) TEM image of the BZCN-A sample.
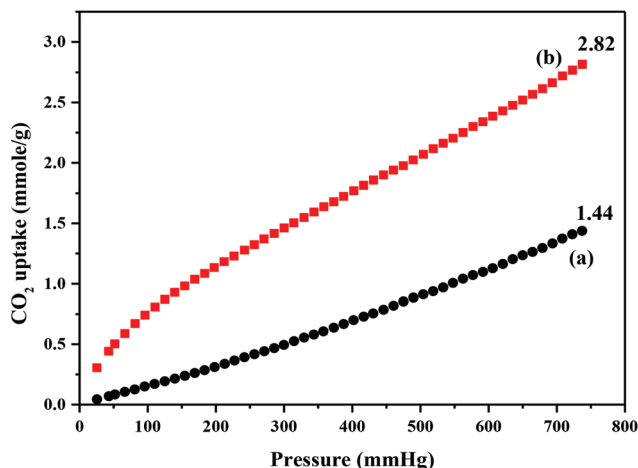
Fig. 12 CO_2 capture using the (a) BZPh-A and (b) BZCN-A samples.

$a = d/(\sqrt{3}/2)$ to be equal to 1.732 nm; thus, the thicknesses of the frameworks of the BZPh-A and BZCN-A microporous carbon materials were approximately 0.05–0.09 nm.

Fig. 12 presents equilibrium CO_2 isotherms, recorded at 25 °C, for the BZPh-A and BZCN-A microporous carbon materials. The CO_2 uptake of the BZPh-A microporous carbon material was only 1.44 mmol g^{-1}; in contrast, it was as high as 2.82 mmol g^{-1} for the BZCN-A microporous carbon material. From the combination of Raman, solid state NMR, XPS, and TEM analyses, we understand that the BZCN-A sample possesses higher N concentration or larger surface area relative to the BZPh-A sample, the higher CO_2 uptake for the BZCN-A microporous carbon material was expected that due to presumably related to these two factors which could enhance the adsorption of acidic CO_2 gas effectively. In addition, this higher value is close to those recorded for other N-containing carbon materials.[39–41,47–49]

Conclusions

We have successfully synthesized two benzoxazine monomers, BZCN and BZPh, through facile Mannich condensations, with their structures were confirmed from FTIR and NMR spectra. DSC and temperature-dependent FTIR spectroscopic analyses show the thermal curing behavior of these benzoxazine monomers, with the CN groups further transforming into triazine rings through thermal polymerization at higher temperatures, thereby forming an additional extended 2D framework that further increased the crosslinking density and N concentrations in the BZCN-type polybenzoxazine. Accordingly, the nitrile-functionalized polybenzoxazine exhibited enhanced thermal properties and a greater cross-linking density after thermal curing, relative to those of the other (non-nitrile) polybenzoxazine. Further carbonization and KOH activation of these two different types of polybenzoxazines resulted in different microporous structures, surface areas, and N atom contents for their two highly ordered microporous N-doped

carbon materials. The BZCN-A microporous carbon material performed better at CO_2 capture because its N atom content (or surface area) was greater than that of the BZPh-A microporous carbon material, thereby enhancing the effective adsorption of acidic CO_2 gas. Thus, this paper describes the first N-doped microporous carbons synthesized directly with precisely defined functional groups on the benzoxazine monomers.

Acknowledgements

References

1 J. Lee, J. Kim and T. Hyeon, *Adv. Mater.*, 2006, **18**, 2073–2094.
2 A. D. Roberts, X. Li and H. Zhang, *Chem. Soc. Rev.*, 2014, **43**, 4341–4356.
3 J. G. Li and S. W. Kuo, *RSC Adv.*, 2011, **1**, 1822–1833.
4 J. G. Li, Y. D. Lin and S. W. Kuo, *Macromolecules*, 2011, **44**, 9295–9309.
5 M. Li, C. Liu, H. Cao, H. Zhao, Y. Zhang and Z. Fan, *J. Mater. Chem. A*, 2014, **2**, 14844–14851.
6 R. R. Salunkhe, C. Young, J. Tang, T. Takei, Y. Ide, N. Kobayashi and Y. Yamauchi, *Chem. Commun.*, 2016, **52**, 4764–4767.
7 R. R. Salunkhe, J. Tang, N. Kobayashi, J. Kim, Y. Ide, S. Tominaka, J. H. Kim and Y. Yamauchi, *Chem. Sci.*, 2016, **7**, 5704–5713.
8 J. Tang, J. Liu, R. R. Salunkhe, T. Wang and Y. Yamauchi, *Chem. Commun.*, 2016, **52**, 505–508.
9 G. A. Ferrero, A. B. Fuertes and M. Sevilla, *J. Mater. Chem. A*, 2015, **3**, 2914–2923.
10 F. Zheng, Y. Yang and Q. Chen, *Nat. Commun.*, 2014, **5**, 5261.
11 W. Niu, L. Li, X. Liu, N. Wang, J. Liu, W. Zhou, Z. Tang and S. Chen, *J. Am. Chem. Soc.*, 2015, **137**, 5555–5562.
12 N. P. Wickramaratne, J. Xu, M. Wang, L. Zhu, L. Dai and M. Jaroniec, *Chem. Mater.*, 2014, **26**, 2820–2828.
13 B. Ashourirad, P. Arab, T. Islamoglu, K. A. Cychosz, M. Thommes and H. M. El-Kaderi, *J. Mater. Chem. A*, 2016, **4**, 14693–14702.
14 L. Liu, Z. H. Xie, Q. F. Deng, X. X. Hou and Z. Y. Yuan, *J. Mater. Chem. A*, 2017, **5**, 418–425.
15 P. X. Hou, H. Orikasa, T. Yamazaki, K. Matsuoka, A. Tomita, N. Setoyama, Y. Fukushima and T. Kyotani, *Chem. Mater.*, 2005, **17**, 5187–5193.
16 X. Cui, Q. Yang, Y. Xiong, Z. Bao, H. Xing and S. Dai, *Chem. Commun.*, 2017, **53**, 4915–4918.
17 J. Kou and L. B. Sun, *Ind. Eng. Chem. Res.*, 2016, **55**, 10916–10925.
18 Y. Z. Chen, C. Cai, Y. Wang, Q. Xu, S. H. Yu and H. L. Jiang, *Green Chem.*, 2016, **18**, 1212–1217.

19 Y. Wang, B. Fugetsu, Z. Wang, W. Gong, I. Sakata, S. Morimoto, Y. Hashimoto, M. Endo, M. Dresslhaus and M. Torrenes, *Sci. Rep.*, 2017, **7**, 40259.

20 X. Zhang, L. Ma, M. Gan, G. Fu, M. Jin, Y. Lei, P. Yang and M. Yan, *J. Power Sources*, 2017, **340**, 22–31.

21 J. W. F. To, J. He, J. Mei, R. Haghpanah, Z. Chen, T. Kurosawa, S. Chen, W. G. Bae, L. Pan, J. B. H. Tok, J. Wilcox and Z. Bao, *J. Am. Chem. Soc.*, 2016, **138**, 1001–1009.

22 A. Alabadi, H. A. Abbood, Q. Li, N. Jing and B. Tan, *Sci. Rep.*, 2016, **6**, 38614.

23 D. Xu, C. Chen, J. Xie, B. Zhang, L. Miao, J. Cai, Y. Huang and L. Zhang, *Adv. Energy Mater.*, 2016, **6**, 1501929.

24 W. F. Zhang, P. Froimowicz, C. R. Arza, S. Ohashi, Z. Xin and H. Ishida, *Macromolecules*, 2016, **49**, 7129–7140.

25 N. N. Ghosh, B. Kiskan and Y. Yagci, *Prog. Polym. Sci.*, 2007, **32**, 1344–1391.

26 S. Ohashi, J. Kilbane, T. Heyl and H. Ishida, *Macromolecules*, 2015, **48**, 8412–8417.

27 R. Kudoh, A. Sudo and T. Endo, *Macromolecules*, 2010, **43**, 1185–1187.

28 Y. S. Ye, Y. J. Huang, F. C. Chang, Z. G. Xue and X. L. Xie, *Polym. Chem.*, 2014, **5**, 2863–2871.

29 R. C. Lin, M. G. Mohamed, K. C. Hsu, J. Y. Wu, Y. R. Jheng and S. W. Kuo, *RSC Adv.*, 2016, **6**, 10683–10696.

30 W. H. Hu, K. W. Huang and S. W. Kuo, *Polym. Chem.*, 2012, **3**, 1546–1554.

31 C. C. Yang, Y. C. Lin, P. I. Wang, D. J. Liaw and S. W. Kuo, *Polymer*, 2014, **55**, 2044–2050.

32 M. G. Mohamed and S. W. Kuo, *Polymer*, 2016, **8**, 225.

33 F. B. Meng, H. Ishida and X. B. Liu, *RSC Adv.*, 2014, **4**, 9471–9475.

34 M. G. Mohamed, K. C. Hsu and S. W. Kuo, *Polym. Chem.*, 2015, **6**, 2423–2433.

35 H. K. Shih, Y. L. Chu, F. C. Chang, C. Y. Zhu and S. W. Kuo, *Polym. Chem.*, 2015, **6**, 6227–6237.

36 H. K. Fu, C. F. Huang, S. W. Kuo, H. C. Lin, D. R. Yei and F. C. Chang, *Macromol. Rapid Commun.*, 2008, **29**, 1216–1220.

37 J. Liu and H. Ishida, *Macromolecules*, 2014, **47**, 5682–5690.

38 G. P. Hao, W. C. Li, D. Qian, G. H. Wang, W. P. Zhang, T. Zhang, A. Q. Wang, F. Schuth, H. J. Bongard and A. H. Lu, *J. Am. Chem. Soc.*, 2011, **133**, 11378–11388.

39 L. Wan, J. Wang, Y. Sun, C. Feng and K. Li, *RSC Adv.*, 2015, **5**, 5331–5342.

40 L. Wan, J. Wang, L. Xie, Y. Sun and K. Li, *ACS Appl. Mater. Interfaces*, 2014, **6**, 15583–15596.

41 L. Wan, J. Wang, C. Feng, Y. Sun and K. Li, *Nanoscale*, 2015, **7**, 6534–6544.

42 P. Kuhn, M. Antonietti and A. Thomas, *Angew. Chem., Int. Ed.*, 2008, **47**, 3450–3453.

43 A. Vinu, P. Srinivasu, M. Takahashi, T. Mori, V. V. Balasubramanian and K. Ariga, *Microporous Mesoporous Mater.*, 2007, **100**, 20–26.

44 J. G. Li, C. Y. Tsai and S. W. Kuo, *Polymer*, 2014, **6**, 1794–1809.

45 T. V. Reshetenko, L. B. Avdeeva, Z. R. Ismagilov, V. V. Pushkarev, S. V. Cherepanova, A. L. Chuvilin and V. A. Likholobov, *Carbon*, 2003, **41**, 1605–1615.

46 M. Thommes, K. Kaneko, A. V. Neimark, J. P. Olivier, F. Rodriguez-Reinoso, J. Rouquerol and K. S. W. Sing, *Pure Appl. Chem.*, 2015, **87**, 1051–1069.

47 G. P. Hao, W. C. Li, D. Qian and A. H. Lu, *Adv. Mater.*, 2010, **22**, 853–857.

48 J. Wei, D. Zhou, Z. Sun, Y. Deng, Y. Xia and D. Zhao, *Adv. Funct. Mater.*, 2013, **23**, 2322–2328.

49 J. C. Hicks, J. H. Drese, D. J. Fauth, M. L. Gray, G. Qi and C. W. Jones, *J. Am. Chem. Soc.*, 2008, **130**, 2902–2903.